GEOPHYSICS, VOL. 84, NO. 5 (SEPTEMBER-OCTOBER 2019); P. R753–R766, 12 FIGS., 5 TABLES.
10.1190/GEO2018-0730.1

Three-parameter prestack seismic inversion based on $L_{1\text{-}2}$ minimization

Lingqian Wang[1], Hui Zhou[1], Yufeng Wang[1], Bo Yu[1], Yuanpeng Zhang[1], Wenling Liu[2], and Yangkang Chen[3]

ABSTRACT

Prestack inversion has become a common approach in reservoir prediction. At present, the critical issue in the application of seismic inversion is the estimation of elastic parameters in the thin layers and weak reflectors. To improve the resolution and the accuracy of the inversion results, we introduced the difference of L_1 and L_2 norms as a nearly unbiased approximation of the sparsity of a vector, denoted as the L_{1-2} norm, to the prestack inversion. The nonconvex penalty function of the L_{1-2} norm can be decomposed into two convex subproblems via the difference of convex algorithm, and each subproblem can be solved efficiently by the alternating direction method of multipliers. Compared with the L_1 norm regularization, the L_{1-2} minimization can reconstruct reflectivities more accurately. In addition, the f-x predictive filtering was introduced to guarantee the lateral continuity of the location and the amplitude of the reflectivity series. The generalized linear inversion and f-x predictive filtering are combined for stable elastic impedance inversion results, and three parameters of P-wave velocity, S-wave velocity, and density can be inverted with the Bayesian linearized amplitude variation with offset inversion. The inversion results of synthetic and real seismic data demonstrate that the proposed method can effectively improve the resolution and accuracy of the inversion results.

INTRODUCTION

Reservoir characteristics, such as lithology, fluidity, and porosity, are important parameters in oil and gas exploration and development. They can be obtained from the P-wave velocity (V_P), S-wave velocity (V_S), and density (ρ) with different petrophysical models (Karimi et al., 2010). Prestack seismic inversion can obtain more elastic parameters than poststack seismic inversion because the amplitude variation with offset (AVO) phenomenon is related to V_P, V_S, and ρ contrasts at an interface between two layers (Aki and Richards, 1980). Like other inverse problems, prestack inversion also suffers difficulties stemming from noise contamination, band limitation, and nonuniqueness (Varela et al., 2006), so it is important to improve the quality of the prestack seismic inversion results by regularization. Some regularization approaches have been proposed to constrain the inverse problem with a priori information to effectively solve the ill-posed problem. Tikhonov (1963) first introduces the regularization method by assuming that the inverted parameters are smooth for a least-squares solution. Buland and Omre (2003) develop a Bayesian AVO inversion method whose objective is to obtain the maximum posterior probability distributions for P-wave velocity, S-wave velocity, and density, and the solutions of the AVO inversion are the posterior Gaussian probability distribution. Karimi et al. (2010) introduce Bayesian closed-skew Gaussian inversion defined as a generalization of traditional Bayesian Gaussian inversion.

Recently, great effort has been made to improve the resolution of the inversion results based on a sparsity assumption. In general, prestack inversion techniques for high resolution are roughly classified into two categories: stochastic and deterministic inversion approaches, each having its own merits and demerits. The former category of prestack inversion is being actively investigated. The priori knowledge is derived from multivariate geostatistical modeling (González et al., 2008; Hansen et al., 2012; Connolly and

Manuscript received by the Editor 23 October 2018; revised manuscript received 21 April 2019; published ahead of production 5 June 2019; published online 24 August 2019.
[1]China University of Petroleum, State Key Laboratory of Petroleum Resources and Prospecting, CNPC Key Lab of Geophysical Exploration, Changping, Beijing 102249, China. E-mail: wanglingqian@live.com; huizhou@cup.edu.cn; hellowangyf@163.com; zghyzcd@163.com; 18829041392@163.com.
[2]CNPC, Research Institute of Petroleum Exploration and Development, Xueyuan Road No. 20, Haidian, Beijing 10083, China. E-mail: liuwenling@petrochina.com.cn.
[3]Zhejiang University, School of Earth Sciences, Hangzhou 310027, China. E-mail: yangkang.chen@zju.edu.cn.

Hughes, 2016; Siri and Deutsch, 2018). Stochastic inversions can produce higher resolution results than conventional deterministic inversions and can help delineate thin beds. However, the major disadvantage of stochastic methods is the computational expense. In contrast, the deterministic inversion approach can provide high-resolution inversion results based on the deterministic sparsity constraints in the transform domain (Yuan et al. 2015; She et al. 2018) or the time domain (Alemie and Sacchi, 2011; Pérez et al., 2013; Chai et al., 2014). The L_1 norm optimization framework was introduced into the prestack inversion for resolving thin layers and clearly delineating layer boundaries (Zhang and Castagna, 2011). Recovering sparse signals from linear measurements is also one of the central subjects of compressed sensing (CS) (Donoho, 2006). Here, we introduce the sparse reconstruction in CS into the prestack AVO inversion. The sparse reconstruction is conducted for the sparsest solution to an underdetermined linear system. Because L_0 counts the number of nonzero elements, minimizing the L_0 norm is equivalent to finding the sparse solution. However, it has been proven that it is NP-Hard to solve the optimization problem with the L_0 norm, which means that it would take too much time to obtain the solution.

The convex relaxation techniques, as a kind of method to solve the optimization problem with the L_0 norm, will provide a biased approximate solution to the L_0 minimization. Therefore, the convex relaxation techniques may sometimes yield suboptimal performance. To address this issue, many nonconvex metrics, such as the L_q quasi-norm with $0 < q < 1$ (Chartrand and Yin, 2008), capped L_1 (Zhang, 2010), smoothly clipped absolute deviation (Fan and Li, 2001), have been proposed to better approximate the L_0 norm. Recently, the L_{1-2} norm was widely used in sparse reconstruction; the property to be more approximate to the L_0 norm and the quickness to find a solution have been demonstrated and developed in mathematics (Esser et al., 2013; Lou et al., 2015). Yin et al. (2015) study the analytical and numerical properties of L_{1-2} minimization for sparse representation. The superior performance of the L_{1-2} norm was verified in different applications including oversampled discrete cosine basis, differential absorption optical spectroscopy, and image denoising (Yin et al., 2015). To more appropriately approximate the L_0 norm, Ma et al. (2017a) propose a truncated difference of the L_1 and L_2 norms discarding large magnitude entries in the regularization term and solve the objective function with the difference of convex functions algorithm (DCA). This method has been validated on sparse vector recovery, matrix completion, and magnetic resonance imaging (Ma et al., 2017a). To improve the computational efficiency of the L_{1-2} minimization, Lou and Yan (2016) incorporate the proximal operator into forward-backward splitting and the alternating direction method of multipliers (ADMM). Recently, the L_{1-2} norm has been used in geophysics. Wang et al. (2018) perform seismic attenuation compensation via first solving the sparse reflectivity series and then convolving them with the seismic wavelet to obtain the seismic record, rather than solving directly for the compensated seismic record. They compensate the seismic record based on the stability and effective computation of the sparse reconstruction.

In this paper, we introduce the L_{1-2} minimization to the prestack reflectivity reconstruction in terms of the sparsity of the reflectivity series in the time domain. We study the ability to reconstruct the relative weak and close reflectivities with L_{1-2} minimization and demonstrate the performance to estimate the thin beds and relative weak reflection interfaces compared with L_1 minimization. The L_{1-2} minimization is divided into two stages. First, the original nonconvex L_{1-2} norm objective function is decomposed into two convex subproblems via DCA (Tao and An, 1998; Liu and Pong, 2017). Second, each subproblem is efficiently solved by ADMM (Yin et al., 2015).

In most cases, the inversion method does not consider the lateral continuity of layers. When the results are combined to form an image profile, the trace-by-trace inversion results may be noisy and important geologic features may be masked (Hamid and Pidlisecky, 2015; Hamid et al., 2018). To reduce and even eliminate these defects in the single-trace processing mode, a series of lateral constraints has been used in seismic inversion and linearized AVO inversion. Many researchers have provided functionality for incorporating different types of geologic information to impose spatial smoothness constraints in their inversion algorithm frameworks (Delprat-Jannaud and Lailly, 1992; Zhang et al., 2013; Karimi, 2015; Huang et al., 2017a; Huo et al., 2017; Ma et al., 2017b). The major disadvantage of the methodology of reforming the objective function to improve the lateral continuity is that it is computationally expensive because of the expansion of the coefficient matrix. Transforming the reflectivities to impedance will magnify the lateral discontinuity associated with the different accuracies of the reflectivity reconstruction for different traces. The reconstruction accuracy includes the location and the magnitude of reflectivities. We introduce the filtering method to the inversion to efficiently improve the lateral continuity of the inversion results. It is known that the f-x predictive filtering or its variation, i.e., f-x singular spectrum analysis, has been widely used in random noise attenuation (Canales, 1984; Naghizadeh and Sacchi, 2012; Chen and Ma, 2014; Huang et al., 2016) and seismic trace interpolation (Spitz, 1991; Porsani, 1999; Wang, 2002; Huang et al., 2017b) under the assumption that the events are nearly linear with respect to the offset dimension. Here, by assuming that the input seismic trace and the inverted reflectivity exhibit similar spatial continuity, we apply f-x predictive filtering to the reflectivity inversion and combine it with the generalized linear inversion (GLI) to obtain the elastic impedance (EI) with well spatial continuity.

In this paper, the prestack inversion is divided into three parts. First, the reflectivity reconstruction is formulated with the L_{1-2} minimization in the time domain. The solver for the L_{1-2} minimization is provided for efficiently implementing reflectivity inversion in the framework of the unconstrained least-squares inversion, in which the DCA and ADMM algorithms are, respectively, used for decomposing the nonconvex problem into two convex subproblems. Then, GLI and the f-x predictive filtering are combined to transform the reflectivity series to the EI of different angles for the purpose of improving the lateral continuity. After that, three parameters of V_P, V_S, and ρ can be inverted with the Bayesian linearized AVO inversion. To demonstrate the effectiveness of the proposed inversion scheme, we apply it to synthetic and field data and show the inversion results.

METHOD

Reflectivity inversion

As usual, we rely on the convolutional model of a seismic trace under the assumption that the earth structure can be represented by a series of horizontal layers of constant material properties separated

by planar interfaces (Yilmaz, 2001). Hence, the angle gather can be expressed as

$$\mathbf{b}(\theta_{\text{ia}}) = \mathbf{A}(\theta_{\text{ia}}) * \mathbf{x}(\theta_{\text{ia}}) + \mathbf{n}(\theta_{\text{ia}}), \quad \text{ia} = 1, 2, \ldots, n_a, \quad (1)$$

where θ_{ia} is the incident angle, $\mathbf{b}(\theta_{\text{ia}})$ is a seismic trace, $\mathbf{A}(\theta_{\text{ia}})$ represents the source wavelet corresponding to angle θ_{ia}, $\mathbf{x}(\theta_{\text{ia}})$ is the reflectivity, $\mathbf{n}(\theta_{\text{ia}})$ stands for random noise, $*$ denotes convolution, and n_a is the number of angle gathers. We assume that the wavelet is known and band limited, it is obtained via wavelet extraction based on well log information or perhaps alternatively via the statistical methodology. Equation 1 can be represented in a matrix form of $\mathbf{Ax} = \mathbf{b}$ for a specific incident angle that is omitted for brevity, regardless of the noise:

$$\begin{bmatrix} b_1 \\ b_2 \\ \vdots \\ b_{N-1} \\ b_N \end{bmatrix} = \begin{bmatrix} w_1 & 0 & \cdots & 0 \\ \vdots & w_1 & \ddots & \vdots \\ w_k & \vdots & \ddots & 0 \\ 0 & w_k & \vdots & w_1 \\ \vdots & \ddots & \ddots & \vdots \\ 0 & \cdots & 0 & w_k \end{bmatrix} \begin{bmatrix} x_1 \\ x_2 \\ \vdots \\ x_{N-1} \\ x_N \end{bmatrix}, \quad (2)$$

where $b_i (i = 1, 2, \cdots, N)$ represents the ith sample of the seismic trace, and N is the number of sampling points, $w_i (i = 1, 2, \cdots, k)$ represents the ith sampling point of the wavelet with a length of k.

Due to the noise contamination, band limitation, and nonuniqueness, the numerical inversion for finding $\mathbf{x}$ using equation 2 is an ill-posed problem. To obtain a solution of equation 2, regularization is generally required. The general regularization is equivalent to solve a constrained optimization problem:

$$\begin{aligned} &\min J(\mathbf{x}), \\ &\text{subject to } \mathbf{Ax} = \mathbf{b}, \\ &\Delta_1 \leqslant c(\mathbf{x}) \leqslant \Delta_2, \end{aligned} \quad (3)$$

where $J(\mathbf{x})$ denotes an objective function that is defined to describe the characteristics of $\mathbf{x}$, $c(\mathbf{x})$ is the constraint to the solution, Δ_1 and Δ_2 are the solution intervals that are given based on the prior information. Here, we assume that the reflectivity series is sparse in the time domain. The constrained optimization problem in equation 3 can be expressed as

$$\min \|\mathbf{x}\|_1, \quad \text{subject to } \mathbf{Ax} = \mathbf{b}. \quad (4)$$

The constrained optimization problem in equation 4 can be converted to the unconstrained minimization problem:

$$\min f(\mathbf{x}) := \|\mathbf{Ax} - \mathbf{b}\|_2^2 + \lambda \|\mathbf{x}\|_2, \quad (5)$$

where $\lambda > 0$ is a scalar regularization parameter. The optimization problem represented by equation 5 is also known as a Lasso problem. There are many state-of-the-art algorithms available for Lasso, such as ADMM (Boyd et al., 2011), fixed-point continuation (Hale et al., 2008), the fast iterative shrinkage-thresholding algorithm (FISTA) (Beck and Teboulle, 2009), and split Bregman (Goldstein and Osher, 2009). However, L_1 minimization may sometimes yield a suboptimal solution due to its biased approximation to L_0 norm in the sense that L_1 is dominated by entries with large magnitudes; differently, all nonzero entries have equal contributions to the L_0 norm (Elad, 2010). In general, L_1 minimization has two effects: first, elimination of the insignificant nonzero elements leading to increased sparsity and, second, reduction in the magnitude of the nonzero elements (Jafarpour et al., 2009). These characteristics lead to the miss of weak reflectivities and the mask of the thin beds. To address this issue, many nonconvex metrics have been proposed to better approximate L_0. Here, we replace the L_1 penalty by a novel L_{1-2} norm in equation 5. The objective function for L_{1-2} regularized reflectivity inversion can be written as

$$\min_{\mathbf{x}} \frac{1}{2} \|\mathbf{Ax} - \mathbf{b}\|_2^2 + \lambda(\|\mathbf{x}\|_1 - \alpha\|\mathbf{x}\|_2), \quad (6)$$

where the weight parameter α in the range of [0,1] is provided to deal with ill-conditioned matrices when the L_{1-2} minimization fails to obtain a good solution (Lou et al., 2015). The value of $\lambda > 0$ is a scalar regularization parameter. A large value of λ would generate sparse solutions, whereas a small value of λ could make the forward modeling results more consistent with the seismic record. Although many researchers have studied the optimization of the regularization parameters, it remains a complex problem to determine them appropriately (Tikhonov and Glasko, 1965; Clapp et al., 2004; Wang and Sacchi, 2007; Brezinski et al., 2008). In this paper, we do not focus on how to select optimal parameters. However, we optimize them by trial and error. The tuning parameter λ is calibrated in terms of the correlation coefficient between the inversion results and the true models for synthetic tests or the well log data for the field data tests. In equation 6, the L_{1-2} minimization is equivalent to the L_1 minimization when α is assigned to zero. Therefore, the L_1 minimization problem can be seen as a particular case in the L_{1-2} minimization optimization problem.

To intuitively understand the L_{1-2} metric and the meaning that L_{1-2} approximates better to the L_0 to find sparse solution, we plot the images in Figure 1 corresponding to L_1 and L_{1-2} norms of a 2D vector with two elements of x and y. The value of the L_0 norm (Figure 1a) is 0 at the origin, 1 at the axes, and 2 elsewhere. The distribution pattern of the L_{1-2} metric image (Figure 1c) is closer to

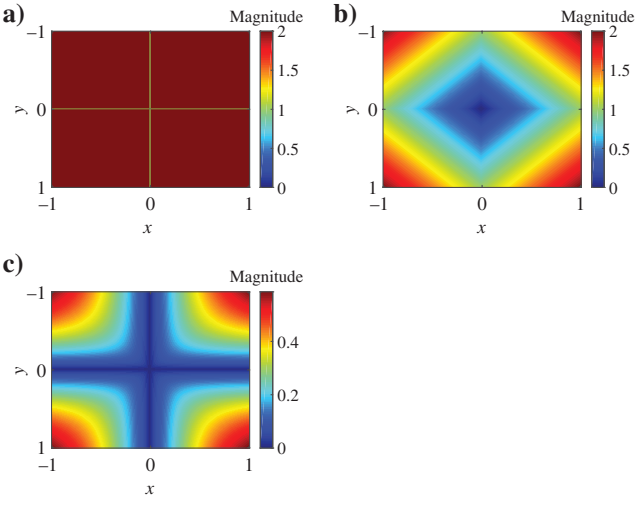

Figure 1. The images of metrics of (a) L_0, (b) L_1, and (c) L_{1-2}.

the L_0 image (Figure 1a) than the L_1 norm (Figure 1b), which indicates that the L_{1-2} metric is better than the L_1 norm in terms of sparsity. Because the distribution pattern of the L_0 norm means that the solution exhibits in the axis for the least nonzero elements. The similar distribution pattern indicates similar sparsity. Therefore, the solution of the L_{1-2} minimization is more approximate to the true sparse solution. Geometrically, minimizing a sparse measure is equivalent to finding an interception of the straight line corresponding to the linear constraints $\mathbf{Ax} = \mathbf{b}$ with a level set of the sparse norm shown in Figure 1. The solution is sparser when the intersection is closer to a coordinate axis. For L_1, it is possible that the straight line coincides with a segment of a level set. In this case, L_1 minimization fails to find a sparse solution. For L_{1-2}, due to its curved level set, the interception is more likely to occur at the coordinate axis. Figure 1 demonstrates that the advantage of the L_{1-2} norm over L_1 is its unbiased characterization of sparse vectors. It is better for the nonconvex constraints to promote sparsity compared with the L_1 norm. However, there is a challenge of computation in a nonconvex optimization problem. Iterative reweighted least-squares as one of the conventional methods to solve the nonconvex minimization may get stuck at a local minimum (Sacchi and Ulrych, 1995). Meanwhile, the conventional nonconvex constraints always have a priori unknown parameters and are non-Lipschitz. Different from them, the L_{1-2} norm is Lipschitz continuous and free of parameters. Therefore, it can be minimized by the DCA without additional smoothing or regularization (Tao and An, 1997). The global minimum can be obtained with DCA empirically. Therefore, the replacement of the L_1 norm with L_{1-2} as the sparsity constraint can improve the accuracy of the solution. Meanwhile, the computational performance can also be guaranteed with DCA. The detailed method to solve the L_{1-2} minimization is shown as follows.

To solve the L_{1-2} minimization, we first decompose the nonconvex L_{1-2} into two convex subproblems via DCA, and then we solve the subproblems of the L_1 norm by ADMM. The DCA is a robust and efficient descent method introduced by Tao and An (1998), which deals with the objective function composed of the difference of two convex functions,

$$F(\mathbf{x}) = G(\mathbf{x}) - H(\mathbf{x}), \tag{7}$$

where $G(\mathbf{x}) = 1/2\|\mathbf{Ax} - \mathbf{b}\|_2^2 + \lambda\|\mathbf{x}\|_1, H(\mathbf{x}) = \alpha\lambda\|\mathbf{x}\|_2$. This algorithm converts the original problem 7 to the calculation of two sequences $\{\mathbf{x}^n\}$ and $\{\mathbf{y}^n\}$ iteratively:

$$\begin{cases} \mathbf{y}^n \in \partial H(\mathbf{x}^n), \\ \mathbf{x}^{n+1} = \min\limits_{\mathbf{x}} G(\mathbf{x}) - (H(\mathbf{x}^n) + \langle \mathbf{y}^n, \mathbf{x} - \mathbf{x}^n \rangle), \end{cases} \tag{8}$$

where $\mathbf{y}^n$ is a subgradient of $H(\mathbf{x})$ at $\mathbf{x}^n$ and is expressed as

$$\mathbf{y}^n = \begin{cases} \mathbf{0}, & \text{if } \mathbf{x}^n = \mathbf{0}, \\ \alpha\lambda \frac{\mathbf{x}^n}{\|\mathbf{x}^n\|_2}, & \text{otherwise.} \end{cases} \tag{9}$$

In each DCA iteration, $\{\mathbf{y}^n\}$ can be obtained directly. Meanwhile, an L_1 regularized convex subproblem

$$\mathbf{x}^{n+1} = \operatorname{argmin}_{\mathbf{x}} \frac{1}{2}\|\mathbf{Ax} - \mathbf{b}\|_2^2 + \lambda\|\mathbf{x}\|_1 + \langle \mathbf{x}, \mathbf{y}^n \rangle \tag{10}$$

is solved to update $\{\mathbf{x}^n\}$.

To transform the original problem into a form that can be solved with ADMM, we introduce an auxiliary variable $\mathbf{z}$ and we redefine the minimization problem as

$$\mathbf{x}^{n+1} = \operatorname{argmin}_{\mathbf{x}} \frac{1}{2}\|\mathbf{Ax} - \mathbf{b}\|_2^2 + \langle \mathbf{y}^n, \mathbf{x} \rangle + \lambda\|\mathbf{z}\|_1, \quad \text{subject to } \mathbf{x} - \mathbf{z} = \mathbf{0}. \tag{11}$$

After applying the augmented Lagrangian multiplier, the minimization problem can be expressed as

$$L_\beta = \frac{1}{2}\|\mathbf{Ax} - \mathbf{b}\|_2^2 + \langle \mathbf{y}^n, \mathbf{x} \rangle + \lambda\|\mathbf{z}\|_1 + \boldsymbol{\omega}^T(\mathbf{x} - \mathbf{z}) + \frac{\beta}{2}\|\mathbf{x} - \mathbf{z}\|_2^2, \tag{12}$$

where $\beta > 0$ is a penalty parameter, $\boldsymbol{\omega}$ is the Lagrange multiplier. The augmented term is the square penalty term of $(\beta/2)\|\mathbf{x} - \mathbf{z}\|_2^2$.

The unconstrained problem in equation 12 can be solved efficiently by ADMM, which consists of the following steps of the $l + 1$th inner iteration of ADMM:

$$\begin{cases} \mathbf{x}^{l+1} = (\mathbf{A}^T\mathbf{A} + \beta\mathbf{I})^{-1}(\mathbf{A}^T\mathbf{b} - \mathbf{y}^n + \beta\mathbf{z}^l - \boldsymbol{\omega}^l), \\ \mathbf{z}^{l+1} = S(\mathbf{x}^{l+1} + \boldsymbol{\omega}^l/\beta, \lambda/\beta), \\ \boldsymbol{\omega}^{l+1} = \boldsymbol{\omega}^l + \beta(\mathbf{x}^{l+1} - \mathbf{z}^{l+1}). \end{cases} \tag{13}$$

In the proposed DCA + ADMM algorithm to solve L_{1-2} minimization, there are two layers of iterations: the outer DCA loop and the inner ADMM loop. Their stopping condition of DCA and ADMM is the same:

$$\left(\frac{\|\mathbf{x}^{k+1} - \mathbf{x}^k\|}{\max\{\|\mathbf{x}^{k+1}\|_2, \|\mathbf{x}^k\|_2\}} \leq \varepsilon \right) \cup (k > M), \tag{14}$$

where $\varepsilon > 0$ is a given tolerance to control the circulation and M is the maximum number of iterations.

Elastic impedance inversion

The reflectivity series can describe the layer boundaries, but it has no information of the elastic parameters. It is necessary to transform the reflectivity series to impedance and then to other parameters to evaluate reservoirs. Much effort has been made to solve the deconvolution problem effectively and accurately. The inverted reflectivity can be substituted into one of the standard recursion formulas to obtain the impedance. However, the results of these recursion schemes are sensitive to the error of the inverted reflectivity series and the accuracy of the EI of the first sample determined from the initial model. The relationship between the reflection coefficients and the EI is linearized by assuming that the absolute values of reflection coefficients are small. For the purpose of improving the lateral continuity of the inversion results, we combine *f-x* predictive filtering and the GLI method.

The most popular seismic inversion technique being used is recursive inversion. The reflectivity at the ith sampling point can be expressed as the following function of $\mathrm{EI}_i(\theta)$ and $\mathrm{EI}_{i+1}(\theta)$:

$$R_i(\theta, \mathrm{EI}_i, \mathrm{EI}_{i+1}) = \frac{\mathrm{EI}_{i+1}(\theta) - \mathrm{EI}_i(\theta)}{\mathrm{EI}_{i+1}(\theta) + \mathrm{EI}_i(\theta)}, \tag{15}$$

by which $\mathrm{EI}_{i+1}(\theta)$ at an incident angle of θ is obtained by a given reflection coefficient $R_i(\theta, \mathrm{EI}_i, \mathrm{EI}_{i+1})$ and its adjacent elastic impedance $\mathrm{EI}_i(\theta)$. Equation 15 can be rewritten to express $\mathrm{EI}_{i+1}(\theta)$ in terms of $R_i(\theta, \mathrm{EI}_i, \mathrm{EI}_{i+1})$ and $\mathrm{EI}_i(\theta)$:

$$\mathrm{EI}_{i+1}(\theta) = \frac{\mathrm{EI}_i(\theta)[1 + R_i(\theta, \mathrm{EI}_i, \mathrm{EI}_{i+1})]}{1 - R_i(\theta, \mathrm{EI}_i, \mathrm{EI}_{i+1})}. \tag{16}$$

The extended recursive inversion to all samples is expressed as

$$\mathrm{EI}_N(\theta) = \mathrm{EI}_1(\theta) \prod_{i=2}^{N} \frac{1 + R_{i-1}(\theta, \mathrm{EI}_{i-1}, \mathrm{EI}_i)}{1 - R_{i-1}(\theta, \mathrm{EI}_{i-1}, \mathrm{EI}_i)}. \tag{17}$$

Expanding equation 17 using the Taylor series and truncating the high-order terms, we obtain the reflectivity at the ith sampling point:

$$R_i(\theta, \mathrm{EI}_i, \mathrm{EI}_{i+1}) = R_i^0(\theta, \mathrm{EI}_i^0, \mathrm{EI}_{i+1}^0) + \frac{\partial R_i(\theta, \mathrm{EI}_i^0, \mathrm{EI}_{i+1}^0)}{\partial \mathrm{EI}_i} \delta \mathrm{EI}_i(\theta) + \frac{\partial R_i(\theta, \mathrm{EI}_i^0, \mathrm{EI}_{i+1}^0)}{\partial \mathrm{EI}_{i+1}} \delta \mathrm{EI}_{i+1}(\theta), \tag{18}$$

where $R_i^0(\theta, \mathrm{EI}_i^0, \mathrm{EI}_{i+1}^0)$ can be obtained with the initial low-frequency EI based on well log information, $\delta \mathrm{EI}_i(\theta) = \mathrm{EI}_i(\theta) - \mathrm{EI}_i^0(\theta)$ is the correction of the initial EI model. Here, $R_i(\theta, \mathrm{EI}_i, \mathrm{EI}_{i+1})$ denotes the reflectivity series obtained with L_{1-2} minimization. We can correct the initial EI model iteratively. The matrix form of equation 18 can be expressed as

$$\begin{bmatrix} \delta R_1(\theta, \mathrm{EI}_1, \mathrm{EI}_2) \\ \delta R_2(\theta, \mathrm{EI}_2, \mathrm{EI}_3) \\ \vdots \\ \delta R_{N-1}(\theta, \mathrm{EI}_{N-1}, \mathrm{EI}_N) \end{bmatrix} = \mathbf{A}_E \begin{bmatrix} \delta \mathrm{EI}_1(\theta) \\ \delta \mathrm{EI}_2(\theta) \\ \vdots \\ \delta \mathrm{EI}_{N-1}(\theta) \\ \delta \mathrm{EI}_N(\theta) \end{bmatrix}, \tag{19}$$

where

$$\mathbf{A}_E = \begin{bmatrix} \frac{\partial R_1(\theta, \mathrm{EI}_1, \mathrm{EI}_2)}{\partial \mathrm{EI}_1} & \frac{\partial R_1(\theta, \mathrm{EI}_1, \mathrm{EI}_2)}{\partial \mathrm{EI}_2} & 0 & \cdots & 0 \\ 0 & \frac{\partial R_2(\theta, \mathrm{EI}_2, \mathrm{EI}_3)}{\partial \mathrm{EI}_2} & \frac{\partial R_2(\theta, \mathrm{EI}_2, \mathrm{EI}_3)}{\partial \mathrm{EI}_3} & \cdots & 0 \\ \cdots & \cdots & \cdots & \cdots & \cdots \\ 0 & \cdots & 0 & \frac{\partial R_{N-1}(\theta, \mathrm{EI}_{N-1}, \mathrm{EI}_N)}{\partial \mathrm{EI}_{N-1}} & \frac{\partial R_{N-1}(\theta, \mathrm{EI}_{N-1}, \mathrm{EI}_N)}{\partial \mathrm{EI}_N} \end{bmatrix}. \tag{20}$$

The stopping criterion for GLI is the same as for DCA and ADMM shown in equation 14. By introducing the low-frequency model obtained from well log data, seismic velocity analysis, or a kriging estimation may improve the lateral continuity of the inversion result of the EI and reduce the local anomaly in the inverted result. However, there may be no obvious improvement for the thin layers because the GLI method does not take into account the lateral continuity of the relatively high-frequency term of the EI.

The characteristic, which a seismic event is predictable in the frequency domain under the linear assumption that seismic events are continuous in space, has been applied widely to random noise attenuation and seismic trace interpolation (Canales, 1984; Spitz, 1991). Here, we want to use this property to suppress the discontinuity of inverted reflectivity series by applying an f-x predictive filter.

Assuming that the inverted reflectivity is a linear function of x, thus, the reflectivity in the t-x domain can be expressed as

$$R(t, h+1) = R(t - h\psi\Delta x, 1), \tag{21}$$

where ψ stands for the slope of the linear reflectivity series, Δx denotes the trace interval, and h represents the trace number changing from 1 to N_{tr}. After Fourier transformation, equation 21 can be expressed in the frequency domain as

$$\tilde{R}(f, h+1) = \tilde{R}(f, 1) \exp(-i2\pi f h \psi \Delta x) = a(f, 1)\tilde{R}(f, h), \tag{22}$$

where $a(f, 1) = \exp(-i2\pi f h \psi \Delta x)$ represents one-step predictor and $\tilde{R}(f, h)$ stands for the Fourier transform of the reflectivity series of the hth trace.

This recursion is an autoregressive (AR) model of first order because the predictive value is known in advance. The first order means that the reflectivity series of a trace is predicted with only one known trace. The extension of the first-order AR model to the pth-order AR model, which predicts the reflectivity series of one trace with p knowns, is represented as

$$\tilde{R}(f, h+1) = \sum_{i=1}^{p} a(f, i)\tilde{R}(f, h+1-i), \tag{23}$$

where $a(f, i)(i = 1, 2, \cdots, p)$ is the predictive filter. There are p unknowns to be solved. By predicting p more traces, overdetermined equations are constructed to obtain the filtering operator $a(f, i)$. In terms of the assumption on the linear continuity of the events, the tuning parameter p should be determined based on the actual seismic records. The tuning parameter p is large when the seismic record is simple and the events are obviously linear. And it is small when the events in the seismic record are complicated. In the following tests, the turning parameter p for f-x filtering is relatively small to avoid eliminating the effective reflectivity at the cost of a relative large amount of computation. Here, we take forward and backward AR modeling into account to predict the reflection profile. With the f-x prediction filter of length L, the prediction equation is

$$\tilde{R}_h(f) = \sum_{j=1}^{L} a_j(f)\tilde{R}'_{h-j}(f), h = L+1, L+2, \cdots, N_{tr}, \tag{24}$$

$$\tilde{R}^*_h(f) = \sum_{j=1}^{L} a'_j(f)\tilde{R}'_{h+j}(f), \quad h = 1, 2, \cdots, N_{tr} - L, \tag{25}$$

where $\tilde{R}_h(f)$ and $\tilde{R}^*_h(f)$ represent the frequency-domain reflectivity after forward and backward f-x predictive filtering from the original reflectivity series $\tilde{R}_h(f)$, $a(f)$ is the forward predictive filter, and $a'(f)$ is the backward predictive filter. After the forward and backward filtering, we take the average of the forward and backward predictive results as the final predictive result.

Our method to transform the reflectivity series to EI consists of three steps:

Step 1: Apply the forward and backward f-x predictive filter to the reconstructed reflectivity series using equations 24 and 25, and take the filtered reflectivity series as the input of GLI.

Step 2: Calculate the reflectivity series of the initial EI model, and calculate the correction of the initial model with equation 19 and update the initial model.

Step 3: Repeat step 2 and take the updated model as the initial model in step 2 until the updated amount meets the requirement.

Due to the predictable property of the reflectivity series, which is the same as that of the seismic trace, the lateral coherency of the final reflectivity profile can be improved by the f-x predictive filter. As a result, the inverted EI obtained by combining GLI and f-x predictive filtering can be improved.

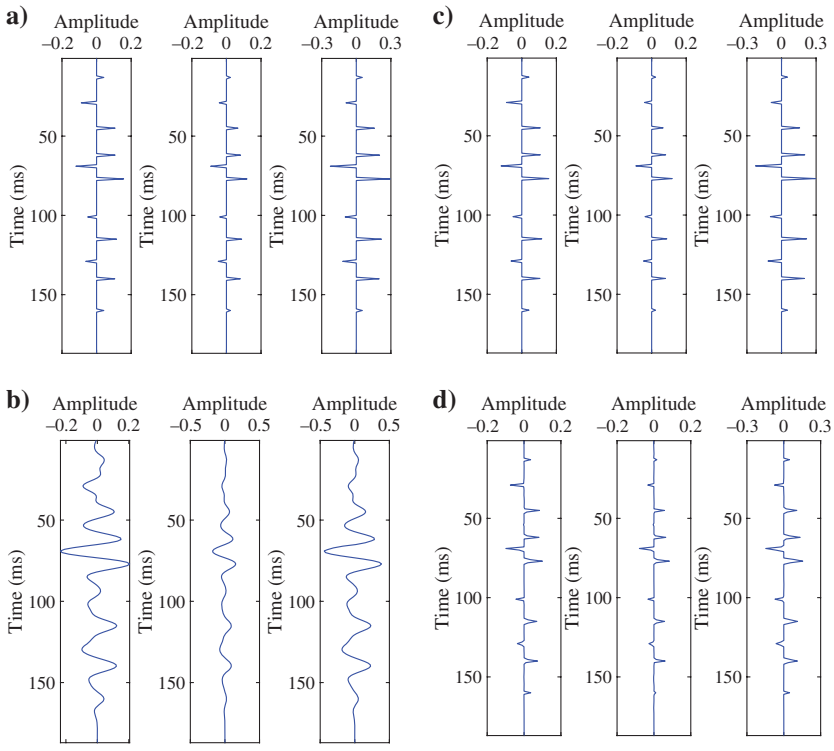

Figure 2. (a) True reflectivity series, (b) noise-free record, (c) reconstructed reflectivity with L_{1-2} minimization, (d) reconstructed reflectivity with L_1 minimization. The left, middle, and right plots in each panel show the information at an angle of 0°, 15°, and 30°, respectively.

Table 1. The correlation coefficient between the true and reconstructed reflectivity by L_1 and L_{1-2} minimization from the noise-free seismic records.

Minimization	Reflectivity of 0°	Reflectivity of 15°	Reflectivity of 30°
L_1	0.9530	0.9685	0.8806
L_{1-2}	0.9964	0.9995	0.9959

AVO inversion for three parameters

The EI is expressed by (Connolly 1998, 1999)

$$\mathrm{EI}(\theta) = V_P^a V_S^b \rho^c, \tag{26}$$

where

$$a=1+\tan^2\theta,\ b=-8K\sin^2\theta,\ c=1-4K\sin^2\theta,\ K=(V_S/V_P)^2. \tag{27}$$

If we have EI corresponding to n_a ($n_a \geq 3$) angle gathers, three parameters of V_P, V_S, and ρ can be inverted, and their relationship can be expressed in a matrix form as

$$\begin{pmatrix} \ln \mathrm{EI}(\theta_1) \\ \ln \mathrm{EI}(\theta_2) \\ \vdots \\ \ln \mathrm{EI}(\theta_{n_a}) \end{pmatrix} = \begin{pmatrix} 1+\tan^2\theta_1 & -8K\sin^2\theta_1 & 1-4K\sin^2\theta_1 \\ 1+\tan^2\theta_2 & -8K\sin^2\theta_2 & 1-4K\sin^2\theta_2 \\ \vdots & \vdots & \vdots \\ 1+\tan^2\theta_{n_a} & -8K\sin^2\theta_{n_a} & 1-4K\sin^2\theta_{n_a} \end{pmatrix} \begin{pmatrix} \ln V_P \\ \ln V_S \\ \ln \rho \end{pmatrix}. \tag{28}$$

Equation 28 is a general matrix form to relate three unknowns of $\ln V_P, \ln V_S, \ln \rho$ to n_a measurements of $\ln \mathrm{EI}(\theta_1), \ln \mathrm{EI}(\theta_2), \cdots, \ln \mathrm{EI}(\theta_{n_a})$. In general, K can be calculated through the low-frequency model. The practical problem is that the coefficient matrix of equation 28 is poorly conditioned unless the angle spacing is sufficiently large. However, the angle range is small in practical applications. There are two reasons why this angle range is small. First, the convolutional model does not work for the seismic data of large offsets; it is only valid for the plane-wave propagation in isotropic layered media with no geometry spread, no scattering and transmission loss, no mode converted wave, and no multiples (Mallick, 2001). Second, the difference between the true reflectivity of the Zoeppritz equations and AVO/EI equations will be greater with the increasing incident angle. To obtain a unique and stable solution of the ill-posed problem, we invert the three parameters based on the Bayesian rule. We compute the solution efficiently with a statistical model based on the maximum a posteriori estimation.

First, we expand the solution of a single point to a single trace based on the EI of different angles:

$$\begin{bmatrix} \ln \mathbf{EI}_1 \\ \ln \mathbf{EI}_2 \\ \vdots \\ \ln \mathbf{EI}_{n_a} \end{bmatrix} = \begin{bmatrix} \mathbf{A}_1 & \mathbf{B}_1 & \mathbf{C}_1 \\ \mathbf{A}_2 & \mathbf{B}_2 & \mathbf{C}_2 \\ \vdots & \vdots & \vdots \\ \mathbf{A}_{n_a} & \mathbf{B}_{n_a} & \mathbf{C}_{n_a} \end{bmatrix} \begin{bmatrix} \ln \mathbf{V}_P \\ \ln \mathbf{V}_S \\ \ln \boldsymbol{\rho} \end{bmatrix}, \tag{29}$$

where $\ln \mathbf{EI}_i$ is the logarithm of the EI of the ith angle, $\ln \mathbf{V}_P$, $\ln \mathbf{V}_S$, and $\ln \boldsymbol{\rho}$ are the logarithms of V_P, V_S, and ρ of a single trace,

$\mathbf{A}_i$, $\mathbf{B}_i$, and $\mathbf{C}_i$ represent the diagonal matrixes of $N \times N$. The coefficient matrix on the right-hand side of equation 29 is denoted as $\mathbf{G}$, the vector on left-hand side is denoted as $\mathbf{d}$, and the vector on the right-hand side is denoted as $\mathbf{m}$. Using the Bayesian rule, the posterior distribution of $\mathbf{m}$ is given by

$$P(\mathbf{m}|\mathbf{d}) = \frac{P(\mathbf{d}|\mathbf{m})P(\mathbf{m})}{P(\mathbf{d})} \propto P(\mathbf{d}|\mathbf{m})P(\mathbf{m}), \tag{30}$$

where $P(\mathbf{d}|\mathbf{m})$ is the likelihood function of the logarithm of the EI, $P(\mathbf{m})$ is the prior distribution, and $P(\mathbf{d})$ is the marginal probability distribution. Assuming the errors of $\mathbf{d}$ are Gaussian with the average value of zero, we express the likelihood function as

$$P(\mathbf{d}|\mathbf{m}) = P_0 \exp[-(2\sigma_n^2)^{-1}(\mathbf{d} - \mathbf{G}\mathbf{m})^T(\mathbf{d} - \mathbf{G}\mathbf{m})], \tag{31}$$

where $P_0 = 1/(2\pi)^{N_{tr}N/2}\sigma_n^{N_{tr}N}$, σ_n is the standard deviation of the errors, which is difficult to determine. In the following tests, the solution is relatively stable due to the sparsity constraints in the reflectivity reconstruction. Therefore, we assign a relatively small value to σ_n to stabilize the solution and avoid smoothing the solution. The Gaussian probability distribution for the prior probability distribution $P(\mathbf{m})$ is given by

$$P(\mathbf{m}) = \frac{1}{(2\pi)^{3N/2}|\sum|^{N/2}} \exp\left[-\frac{1}{2}\sum_{i=1}^{N}(\mathbf{m}_i - \boldsymbol{\mu}_m)^T\boldsymbol{\Sigma}^{-1}(\mathbf{m}_i - \boldsymbol{\mu}_m)\right], \tag{32}$$

where $\boldsymbol{\Sigma}$ is the covariance matrix of 3×3, $\mathbf{m}_i$ is the three parameters at the ith sample point, and $\boldsymbol{\mu}_m$ is the mean of the three parameters from the well log or the low-frequency model. Substitution of equations 31 and 32 into equation 30, after some algebraic operation, the objective function for the maximum posterior probability can be expressed as

$$\min_{\mathbf{m}}(\mathbf{d} - \mathbf{G}\mathbf{m})^T(\mathbf{d} - \mathbf{G}\mathbf{m}) + \sigma_n^2\sum_{i=1}^{N}(\mathbf{m}_i - \boldsymbol{\mu}_m)^T\boldsymbol{\Sigma}^{-1}(\mathbf{m}_i - \boldsymbol{\mu}_m). \tag{33}$$

By solving equation 33, we obtain $\mathbf{m}$, which is the logarithm of V_P, V_S, and ρ, and we finally obtain the inverted V_P, V_S, and ρ by exponentiating the solution $\mathbf{m}$.

EXAMPLES

Synthetic data example

We test the inversion method in three terms in this subsection. First, we compare the performance of our proposed L_{1-2} regularized deconvolution with the L_1 regularized deconvolution for a single trace with different angles. Second, we conduct the L_{1-2} minimization test on a synthetic angle gather with incident angles ranging from 0° to 45°. Third, we use the SEG/EAGE overthrust model to demonstrate the effectiveness of our algorithm in prestack three-parameter inversion.

The first test is conducted on noise-free seismograms. The reflectivity series of 0°, 15°, and 30° are shown in Figure 2a. We use a Ricker wavelet with a dominant frequency of 50 Hz as the source. The seismograms (Figure 2b) are generated by convolving the reflectivity series with the given wavelet. The reflectivity reconstruction results obtained by the L_{1-2} and L_1 regularized deconvolution methods are shown in Figure 2c and 2d, respectively. In this example, we choose a relatively small balancing parameter $\lambda = 5e-4$, $\alpha = 1$ to stabilize the sparse solution, and the weight parameter α is fixed in all of the following tests. Meanwhile, the balancing parameter λ is the same in the L_1 minimization and the L_{1-2} minimization. The two methods can reconstruct the reflectivity series accurately and efficiently

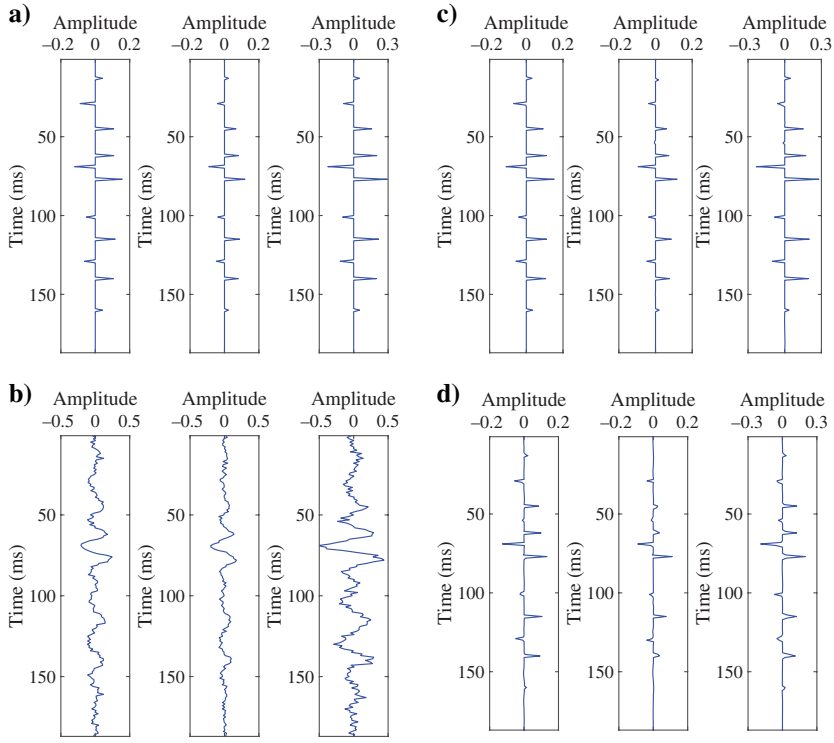

Figure 3. (a) True reflectivity series, (b) noisy record, (c) reconstructed reflectivity with L_{1-2} minimization, and (d) reconstructed reflectivity with L_1 minimization. The left, middle, and right plots in each panel show the information at an angle of 0°, 15°, and 30°, respectively.

Table 2. The correlation coefficient between the true and reconstructed reflectivity by L_1 and L_{1-2} minimization from the noisy seismic records with S/N = 6.

Minimization	Reflectivity of 0°	Reflectivity of 15°	Reflectivity of 30°
L_1	0.7988	0.8121	0.7175
L_{1-2}	0.9326	0.9281	0.9375

in the absence of noise. To illustrate the improvement of the reflectivity reconstruction precision with the L_{1-2} minimization, we use the correlation coefficient between the true and reconstructed reflectivity as the quantitative evaluation. Table 1 shows the correlation coefficient for the noise-free seismic records. The reconstructed reflectivity by the L_1 minimization and the L_{1-2} minimization is acceptable in the absence of noise.

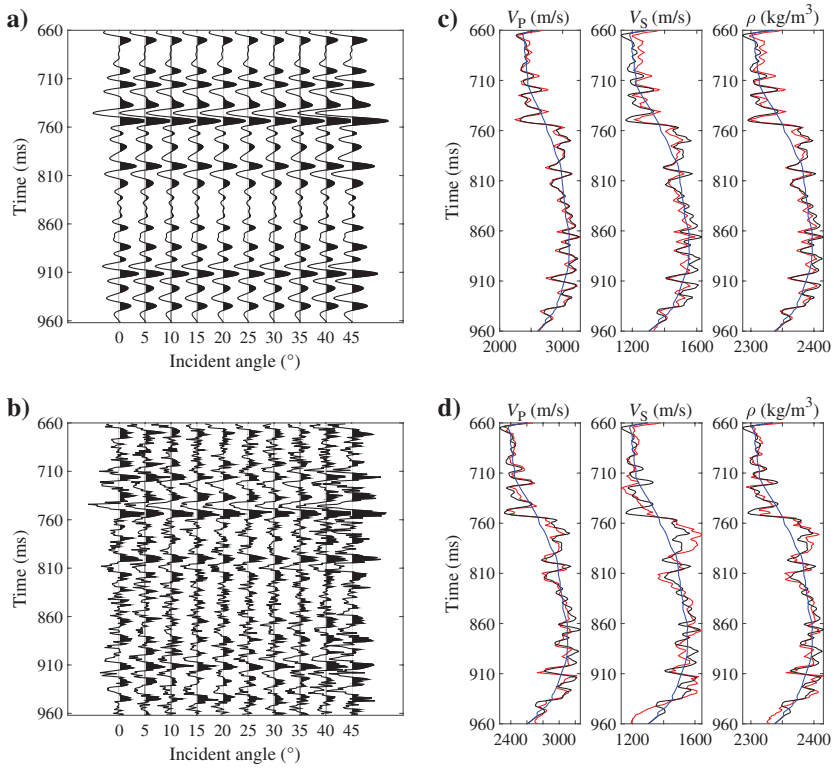

Figure 4. One-dimensional tests applied to a piece of real well log data. (a) The synthetic traces without noise, (b) the noisy synthetic traces with S/N = 2, (c) the inversion results of V_P, V_S, and density (red lines) from noise-free synthetic data, and (d) the inversion results from noisy data of S/N = 2. The low-frequency initial models (blue lines) and the true models (black lines) are also shown in (c and d).

Further, we test the method on a noisy seismic record. Figure 3a shows the exact reflectivity series as the reference, and Figure 3b shows a noisy seismogram with a signal-to-noise ratio (S/N) = 6. The S/N is the ratio of the root-mean-square amplitude of the signal to that of the noise with normal distribution. The inverted results with the L_1 and L_{1-2} norms are shown in Figure 3c and 3d, respectively. In this test, we select a relatively large balancing parameter $\lambda = 8e-3$ in the L_1 and L_{1-2} minimizations to suppress the effect of random noise. The excellent magnitude recovery property of our proposed method is verified when the reflectivity is relatively weak, and the record is embedded in the noise (e.g., the reflectivity at 13 and 160 ms), especially in the 15° reflectivity series with a relatively small magnitude. Meanwhile, the magnitude of the reconstructed reflectivity with the L_1 norm is smaller compared to the true reflectivity such as the reflectivity of 30° at 77 and 129 ms. Table 2 shows the correlation coefficient between the true and reconstructed reflectivity from the noisy seismic record. The correlation coefficient decreases compared with the reconstructed results from the noise-free seismic record. The correlation coefficient between the true and reconstructed reflectivity from the L_{1-2} minimization is larger compared with the reflectivity correlation coefficient from the L_1 minimization. Therefore, the reflectivity can be reconstructed more precisely with the L_{1-2} norm constraint.

We next test the prestack seismic inversion scheme based on the L_{1-2} minimization on a synthetic angle gather with incident angles ranging from 0° to 45° with a gap of 5°. The entire seismic records with different angles are applied to invert the velocities and density. This synthetic angle gather (Figure 4a) is generated by convoluting a wavelet with a 50 Hz dominant frequency extracted from the seismic record with a section of well log data. Figure 4b shows the noisy angle gather with S/N = 2. In this synthetic data inversion test, σ_n is assigned to 10^{-15}, and the tuning parameter $\lambda = 10^{-4}$ is relatively small in the absence of noise, and it is $\lambda = 5 \times 10^{-2}$ in the case of a noisy seismic record with S/N = 2. Figure 4c and 4d displays the inverted V_P, V_S, and ρ (the red lines) from the noise-free synthetic data (Figure 4a) and noisy data (Figure 4b), and the true V_P, V_S, and ρ (black lines), respectively. The initial models are also plotted in Figure 4c and 4d with blue lines, which are the low-pass-filtered well log data. We find that the inversion results match well with the true velocities and density when there is no noise in the data. The inversion results shown in Figure 4d also indicate the stability of the inversion method when we add random Gaussian noise to the synthetic traces. Table 3 lists the correlation coefficient between the true and inverted elastic parameters from the seismic records without and with noise of S/N = 2. We find that the inverted V_S is easier to be

Table 3. The correlation coefficient between the true and the inverted elastic parameters by L_{1-2} minimization from the noise-free and noisy seismic records.

Seismic data	P-wave velocity	S-wave velocity	Density
Noise-free	0.9638	0.9017	0.9476
Noisy	0.8772	0.8281	0.8533

Table 4. The MSE of the estimated elastic parameters from the seismic records with L_1 and L_{1-2} minimization combined with and without f-x filtering.

Minimization	P-wave velocity	S-wave velocity	Density
L_1	2.7050×10^4	1.5696×10^4	784.1338
L_1 with f-x filtering	2.4668×10^4	1.2932×10^4	711.6990
L_{1-2}	2.1970×10^4	8.9134×10^3	492.6038
L_{1-2} with f-x filtering	2.0089×10^4	7.1800×10^3	450.1180

contaminated by random noise and the inverted V_P is more stable and accurate compared with the other two parameters.

As a benchmark model, the SEG/EAGE overthrust model (Figure 5a–5c) is used as an inversion example. The corresponding reflectivity model is computed from the V_P, V_S, and ρ models using the Aki-Richards equation (Aki and Richards, 1980) for the PP reflection coefficient, and then it is convolved with a Ricker wavelet of a dominant frequency 40 Hz, which is discretized with a sample interval of 1 ms to generate a discrete wavelet with 81 samples. Three angle gathers of 0°, 15°, and 30° are applied to invert three parameters. White Gaussian noise is added to the angle gathers to generate the sections with an S/N = 6 (Figure 5d–5f). These sections are used to estimate the V_P, V_S, and ρ models by removing the effect of the wavelet via deconvolution and obtain the three parameters using the Aki-Richards equation. The initial models (Figure 6a–6c) are created by smoothing the true models. In this synthetic test, we set the scalar parameter λ to 5×10^{-3} and the parameter p for f-x filter to 10. The other tuning parameters are the same as the values of the second synthetic data tests. In this synthetic test, we use the mean-square-error (MSE) of the P-wave velocity, S-wave velocity, and density to evaluate the accuracy of the inversion results with L_1 and L_{1-2} minimizations. To illustrate the efficiency of the GLI combined with f-x filtering, we also compare the inversion results with and without f-x filtering, respectively. The inversion results with L_1 minimization combined without and with f-x filtering are shown in Figure 7, and the inversion results with L_{1-2} minimization combined without and with f-x filtering are shown in Figure 8. From the inversion results, we

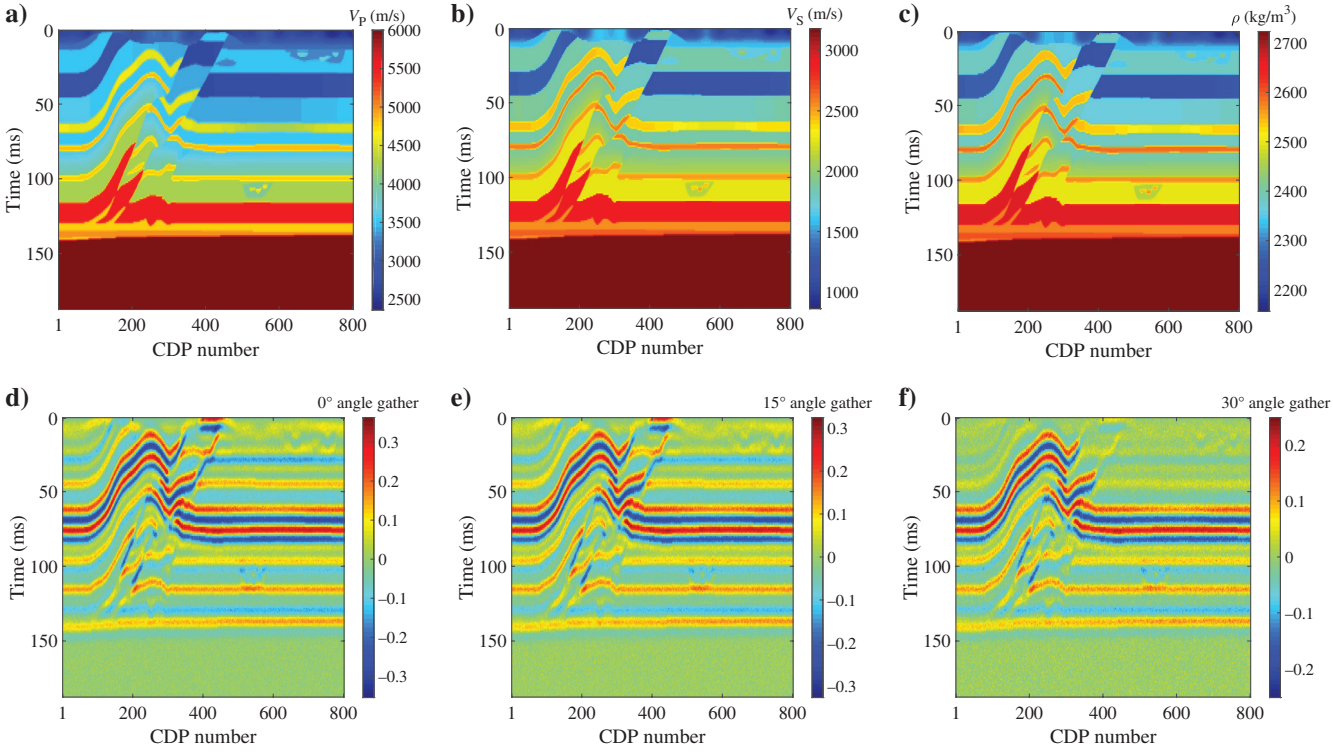

Figure 5. The true SEG/EAGE overthrust model of (a) V_P, (b) V_S, and (c) density. The angle gathers with S/N = 6 of (d) 0°, (e) 15°, and (f) 30°.

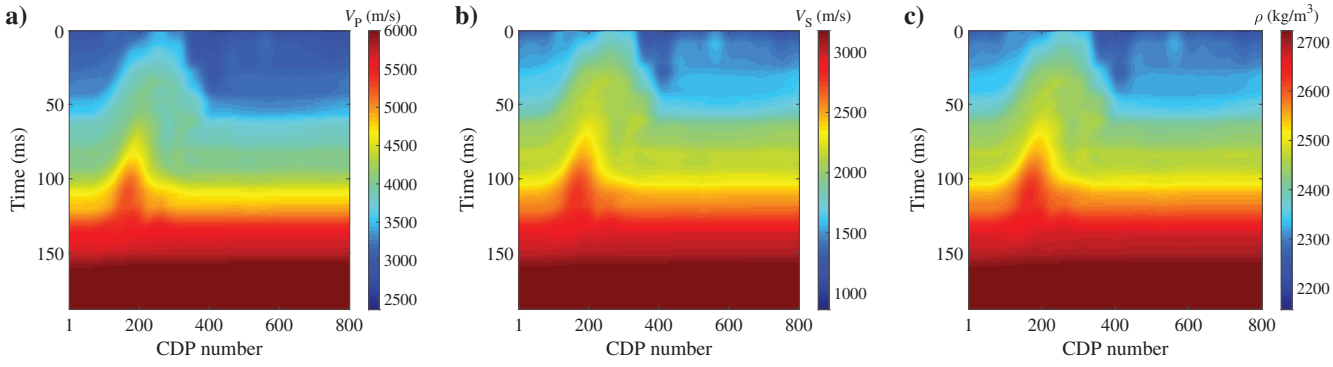

Figure 6. The initial model of (a) V_P, (b) V_S, and (c) density.

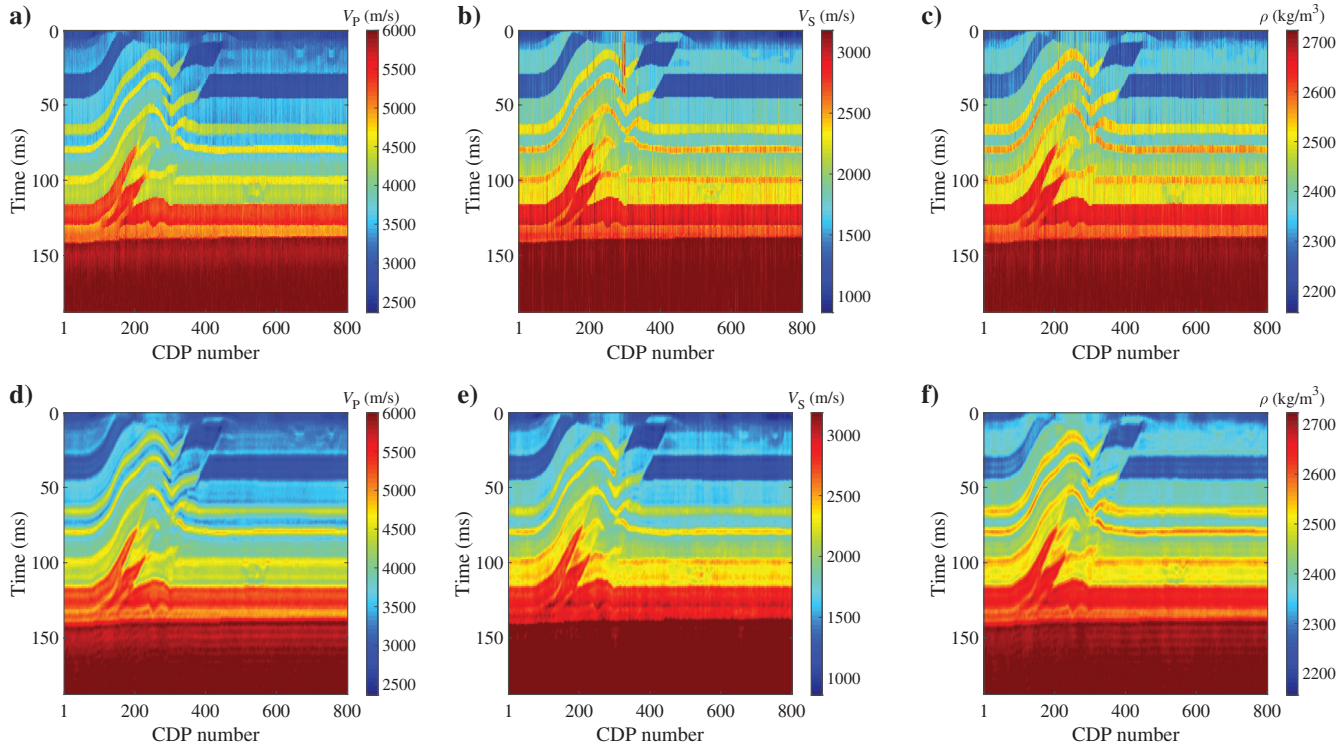

Figure 7. The inversion results of (a) V_P, (b) V_S, and (c) density with L_1 minimization without f-x filtering and (d) V_P, (e) V_S, and (f) density with L_1 minimization combined with f-x filtering.

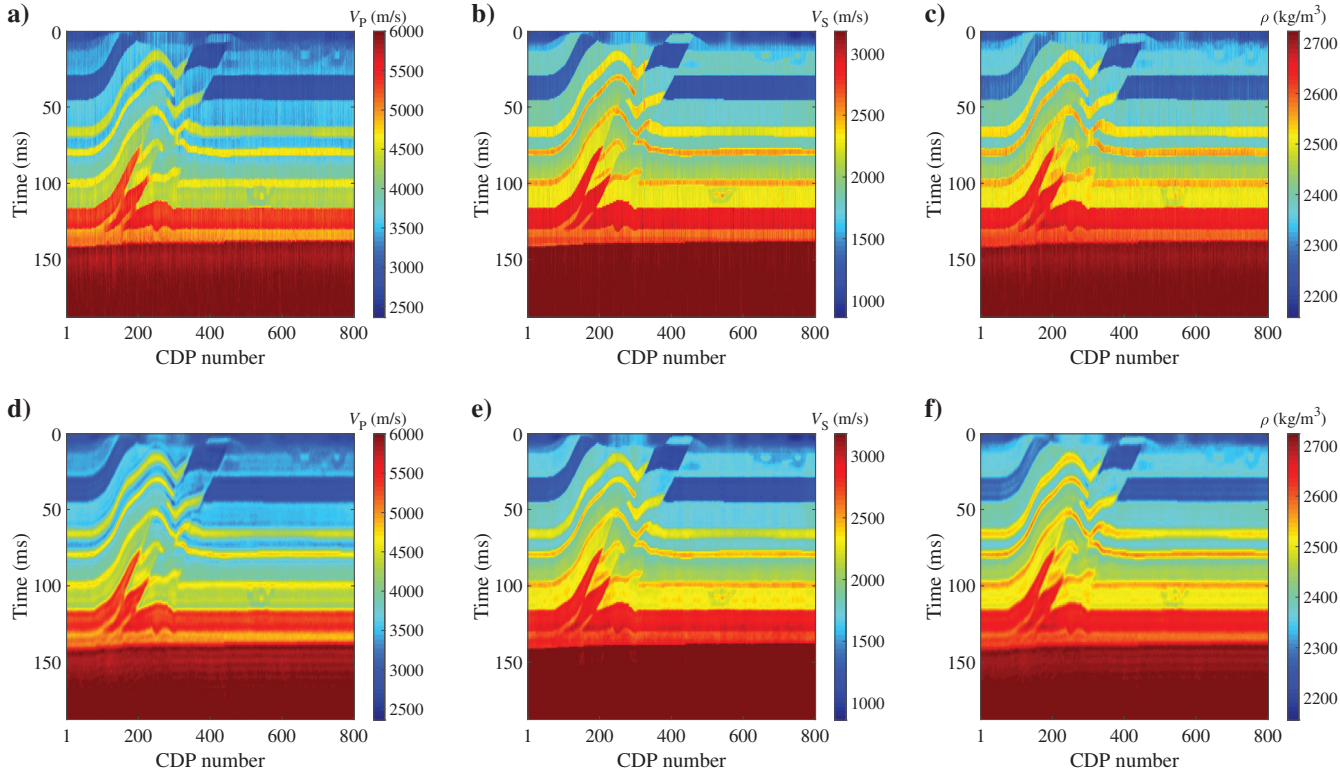

Figure 8. The inversion results of (a) V_P, (b) V_S, and (c) density with L_{1-2} minimization without f-x filtering and (d) V_P, (e) V_S, and (f) density with L_{1-2} minimization combined with f-x filtering.

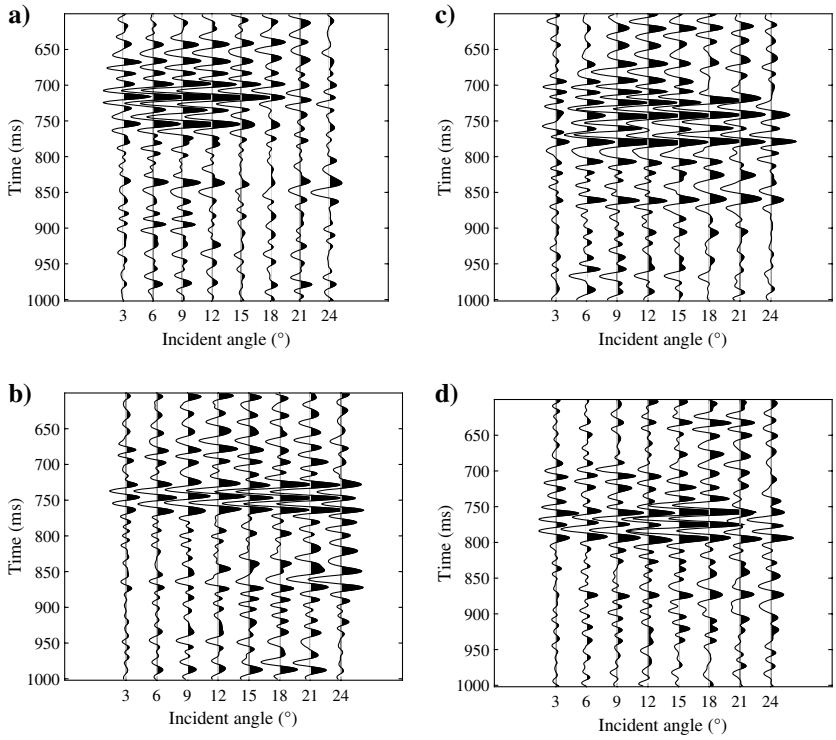

Figure 9. The angle gathers ranging from 3° to 24° at (a) CDP 120, (b) CDP 150, (c) CDP 210, and (d) CDP 260.

can find some small-scale features, such as thin beds and pinch-outs, in the overthrust model. It is shown that the inversion results with f-x filtering can improve the lateral stability effectively. In addition, through the MSE for the four algorithms listed in Table 4, we find that L_{1-2} minimization can obtain more accurate inversion results compared with L_1 minimization and the f-x filtering may not improve the inversion results obviously. However, the f-x filtering can eliminate the trails and improve the lateral continuity obviously in 2D inversion results shown in Figures 7 and 8. The magnitudes of MSE are different in P-wave velocity, S-wave velocity, and density associated with their different ranges of values. To summarize, the L_{1-2} minimization can improve the accuracy of the inversion results compared with L_1 minimization. Meanwhile, f-x filtering can improve the lateral continuity of the inversion results without losing the accuracy.

Field data example

Before prestack inversion is conducted, the original prestack seismic data should be processed mainly with three steps. At first, the noise is suppressed for getting more stable and accurate inversion results. Then, an amplitude compensation is applied for compensating the loss of energy due to

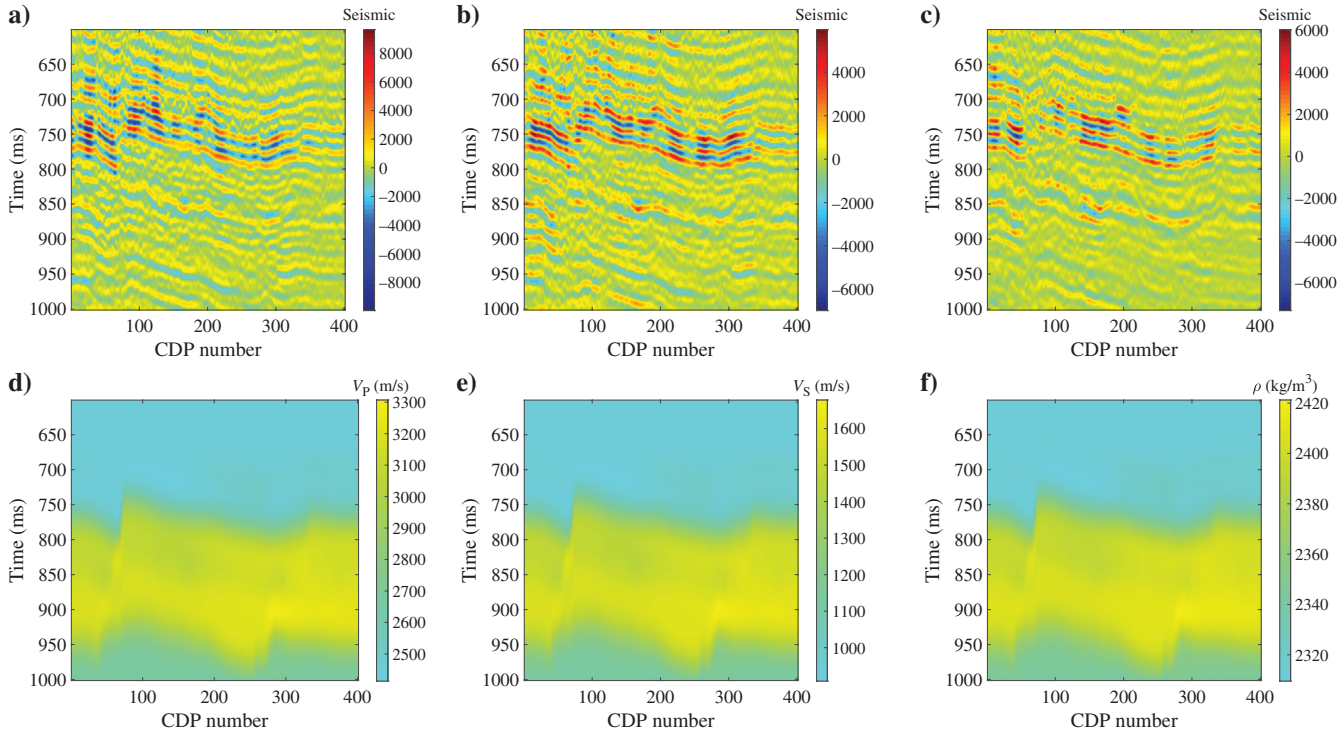

Figure 10. Partially stacked angle profiles of (a) small-angle range, (b) middle-angle range, and (c) large-angle range. The initial model of (d) V_P, (e) V_S, and (f) density.

spherical diffusion and formation absorption in the propagation of the seismic wavelet, and for making sure that the final prestack amplitudes represent the reflection strength of subsurface interfaces as accurately as possible. Finally, the preserved-amplitude prestack migration improves the spatial resolution and the S/N. A small 2D field data set is used for the inversion test. We choose common depth point (CDP) gathers in the time-angle domain of a survey line, on which there are three known wells at CDP 136, CDP 263, and CDP 287. The maximum incident angle is at approximately 24°. Figure 9 shows the angle gathers at different CDPs of 120, 150, 210, and 260. The three wells are used to establish a low frequency (high-cut frequency of 10–15 Hz), initial velocities, and density models as shown in Figure 10d–10f. Figure 10a–10c illustrates the partially stacked angle gathers with small, middle, and large incident angles ranging from 6° to 12°, 12° to 18°, and 18° to 24°, respectively. In the field data test, the optimal λ is 5×10^{-2} and the turning parameter $p = 10$ in terms of the lateral continuity of the seismic events. Figure 11d–11f depicts the inverted P-wave velocity, S-wave velocity, and density with L_{1-2} minimization. To illustrate the advanced performance of our method, we also show the inversion results in Figure 11a–11c based on the model constraint that has been used widely in industry. From the inversion results (Figure 11) and the initial models (Figure 10d–10f), we find that there are rapid varying values of V_P, V_S, and density profiles at 700 and 950 ms caused by the change of the strata. Although the inversion results shown in Figure 11a–11c may reveal the change of the strata, the thin beds cannot be clearly observed. It is obvious that the resolution of the inversion results with our method is improved.

Then, we compare the inversion results (Figure 11d and 11e) with the well logs to evaluate its accuracy. The black lines in Figure 11d–11f represent the location of the well at CDP 136 used for the comparison with well logs. Because the original well log data contain very high-frequency components, they cannot be used directly to make comparison with the inversion results. The well log data are processed by a low-pass filter with high-cut frequency of 70–80 Hz before the comparison is conducted. We should see whether the trends of the inversion results agree with the filtered well log data. Figure 12 shows the original well log data by red lines; low-pass-filtered well log data by black lines; and inverted V_P, V_S, and ρ by blue lines. From Figure 12, we see that the inverted V_P, V_S, and ρ obtained with the L_{1-2} minimization show a good agreement with the known logs after low-pass filtering. Though there are also some mismatches in numerical values between the inversion results and the well log data, they follow the same trend. Table 5 records the correlation coefficient between the filtered well log data and the inverted elastic parameters with L_{1-2} minimization and the inversion results with the model constraint. It is found that the correlation coefficients of three elastic parameters are larger than 0.7, which means that the accuracy of the inversion results is acceptable.

DISCUSSION

The challenge of the inversion of thin layers and a weak reflection interface is associated with the band limitation and noise contamination. The sparsity norm plays an important role in high-resolution

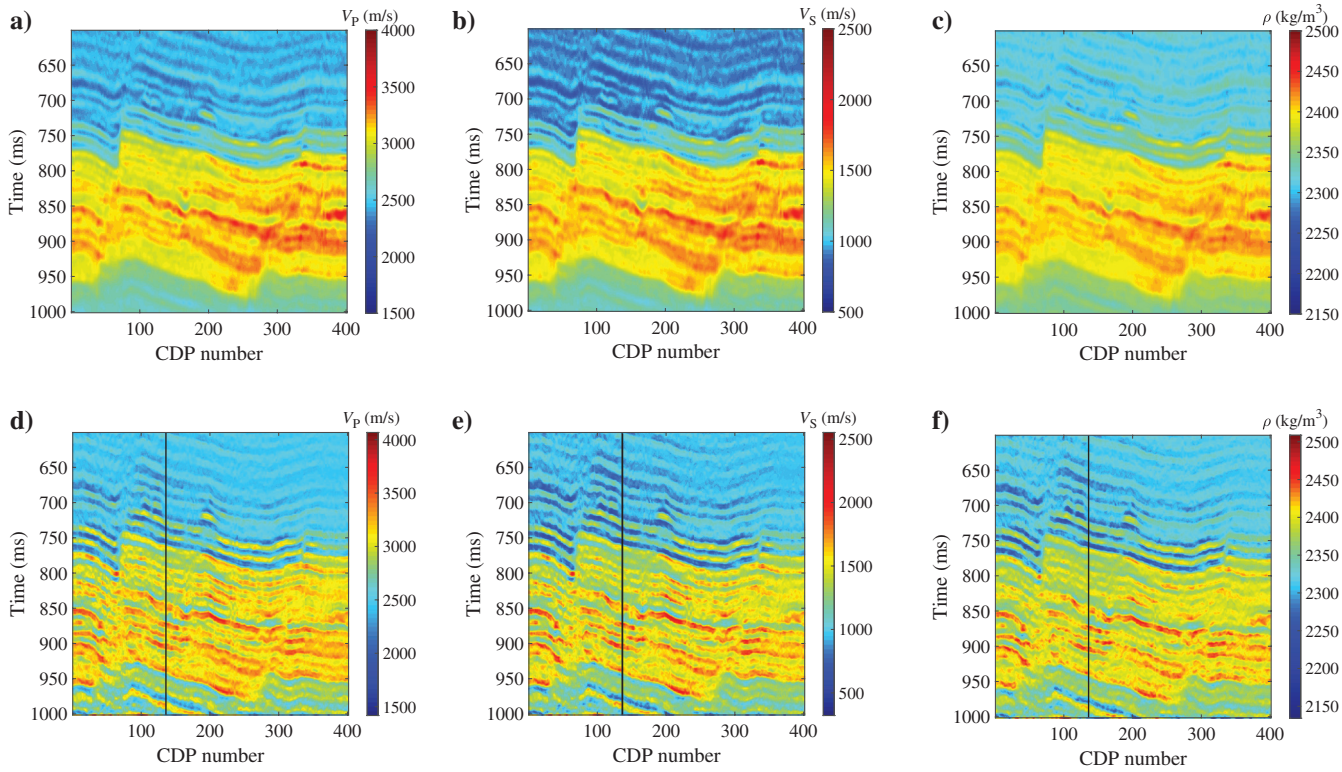

Figure 11. Estimated parameters obtained by the inversion method based on the model constrained. (a) V_P, (b) V_S, and (c) density. The inversion results of (d) V_P, (e) V_S, and (f) density with the proposed inversion approach. The black lines represent the location of the well at CDP 136.

inversion. Zhang et al. (2013) propose a basis pursuit inversion algorithm based on the L_1 norm to resolve sharp boundaries of strata. Because the L_1 norm is dominated with the large absolute value, the relatively weak reflectivities cannot be reconstructed accurately. We should stress that the main point of this paper is to use the L_{1-2} norm in prestack reflectivity reconstruction taking advantage of the unbiased approximation to the L_0 norm. Different from the equal contribution to the L_0 norm of each nonzero element, the L_{1-2} norm as an unbiased approximation to the L_0 norm can provide more accurate and sparser solution including the relative weak reflectivity. Wang et al. (2018) perform seismic attenuation compensation via initially solving sparse reflectivity series and then converting it into the seismic record, rather than directly compensating the seismic record. They study the computational efficiency and convergence of the L_{1-2} minimization. The stability and the wavelet independence of the proposed method have been demonstrated through synthetic tests. In this paper, we mainly study the ability to estimate the thin beds and the weak reflection interfaces with L_{1-2} minimization. It can be considered an extension of the L_{1-2} minimization in Wang et al. (2018) and the sparsity reconstruction of Zhang et al. (2013). As shown in Figure 3, the overall accuracy of L_{1-2} and L_1 minimizations is slightly degraded in the presence of noise. The amplitude of the results with L_1 minimization can hardly reflect the true situations, and the relatively weak reflectivities may be cut away. However, L_{1-2} minimization can accurately reconstruct the location of all reflectivities. In addition, we also introduce the f-x predictive filtering, GLI algorithm, and Bayesian method for a more stable inversion results. The f-x predictive filtering is introduced to guarantee the lateral continuity of the location and the amplitude of the reflectivity series.

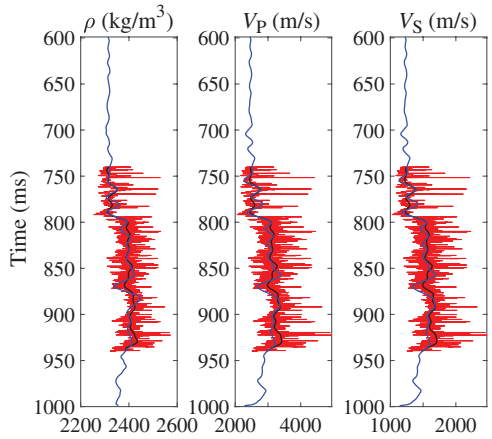

Figure 12. Inverted density, V_P and V_S (blue lines), well log density, V_P and V_S (red lines), and low-pass-filtered results of the well logs (black lines).

Table 5. The correlation coefficient between the well log and the inverted elastic parameters with L_{1-2} minimization and the model constraint from the field data.

Constraint	P-wave velocity	S-wave velocity	Density
Model constrained	0.8237	0.8184	0.7923
L_{1-2} minimization	0.8269	0.8257	0.8094

CONCLUSION

The three-parameter prestack AVO inversion scheme discussed is formulated with the L_{1-2} minimization, the GLI combined with the f-x predictive filtering and the AVO inversion based on the Bayesian inference framework. First, we invert the reflectivity series with the L_{1-2} norm, which is solved with the DCA and the ADMM to obtain a more accurate solution. Second, we combine the GLI and f-x predictive filtering to improve the lateral continuity of the EI corresponding to different angles. We calculate the three parameters of P-wave velocity, S-wave velocity, and density based on the Bayesian inference framework. The advantage of our method is that we take the following factors into account: the sparsity of the reflectivity, the lateral continuity of the subsurface parameters, and the probability distribution of the parameters to be inverted. The inversion tests with synthetic data demonstrate that the inverted results are in good agreement with the true models. The inversion test with real seismic data also shows that the reconstructed velocities and density fit well with the well log measurements and the layer delineation is improved, which provides additional information for subsequent interpretation.

ACKNOWLEDGMENTS

This work was supported in part by the National Key Science and Technology Program (grant no. 2016ZX05010-001), the National Natural Science Foundation of China (grant no. 41630314), and the New Geophysical Technology and Method Project of Deep and Unconventional Seismic of CNPC (grant no. 2016A-3302), and Scientific Research and Development of CNPC (grant no. 2017D-5006-16).

DATA AND MATERIALS AVAILABILITY

Data associated with this research are confidential and cannot be released.

REFERENCES

Aki, K., and P. G. Richards, 1980, Quantitative seismology: Theory and methods: W. H. Freeman.

Alemie, W., and M. D. Sacchi, 2011, High-resolution three-term AVO inversion by means of a Trivariate Cauchy probability distribution: Geophysics, **76**, no. 3, R43–R55, doi: 10.1190/1.3554627.

Beck, A., and M. Teboulle, 2009, A fast iterative shrinkage-thresholding algorithm for linear inverse problems: SIAM Journal on Imaging Sciences, **2**, 183–202, doi: 10.1137/080716542.

Boyd, S., N. Parikh, E. Chu, B. Peleato, and J. Eckstein, 2011, Distributed optimization and statistical learning via the alternating direction method of multipliers: Foundations and Trends in Machine Learning, **3**, 1–122, doi: 10.1561/2200000016.

Brezinski, C., G. Rodriguez, and S. Seatzu, 2008, Error estimates for linear systems with applications to regularization: Numerical Algorithms, **49**, 85–104, doi: 10.1007/s11075-008-9163-1.

Buland, A., and H. Omre, 2003, Bayesian linearized AVO inversion: Geophysics, **68**, 185–198, doi: 10.1190/1.1543206.

Canales, L., 1984, Random noise reduction: 54th Annual International Meeting, SEG, Expanded Abstracts, 525–527, doi: 10.1190/1.1894168.

Chai, X., S. Wang, S. Yuan, J. Zhao, L. Sun, and X. Wei, 2014, Sparse reflectivity inversion for nonstationary seismic data: Geophysics, **79**, no. 3, V93–V105, doi: 10.1190/geo2013-0313.1.

Chartrand, R., and W. Yin, 2008, Variable selection via nonconcave penalized likelihood and its oracle properties: IEEE International Conference on Acoustics, 3869–3872.

Chen, Y., and J. Ma, 2014, Random noise attenuation by f-x empirical-mode decomposition predictive filtering: Geophysics, **79**, no. 3, V81–V91, doi: 10.1190/geo2013-0080.1.
Clapp, R. G., B. Biondi, and J. F. Claerbout, 2004, Incorporating geologic information into reflection tomography: Geophysics, **69**, 533–546, doi: 10.1190/1.1707073.
Connolly, P., 1998, Calibration and inversion of non-zero offset seismic: 68th Annual International Meeting, SEG, Expanded Abstracts, 182–184, doi: 10.1190/1.1820288.
Connolly, P., 1999, Elastic impedance: The Leading Edge, **18**, 438–452, doi: 10.1190/1.1438307.
Connolly, P., and M. Hughes, 2016, Stochastic inversion by matching to large numbers of pseudo-wells: Geophysics, **81**, no. 2, M7–M22, doi: 10.1190/geo2015-0348.1.
Delprat-Jannaud, F., and P. Lailly, 1992, What information on the earth model do reflection travel time provide?: Journal of Geophysical Research, **97**, 19827–19844, doi: 10.1029/92JB01739.
Donoho, D. L., 2006, Compressed sensing: IEEE Transactions on Information Theory, **52**, 1289–1306, doi: 10.1109/TIT.2006.871582.
Elad, M., 2010, Sparse and redundant representations: Springer.
Esser, E., Y. Lou, and J. Xin, 2013, A method for finding structured sparse solutions to nonnegative least squares problems with applications: SIAM Journal on Imaging Sciences, **6**, 2010–2046, doi: 10.1137/13090540X.
Fan, J., and R. Li, 2001, Variable selection via nonconcave penalized likelihood and its oracle properties: Journal of the American Statistical Association, **96**, 1348–1360, doi: 10.1198/016214501753382273.
Goldstein, T., and S. Osher, 2009, The split Bregman method for L1-regularized problems: SIAM Journal on Imaging Science, **2**, 323–343, doi: 10.1137/080725891.
González, E., T. Mukerji, and G. Mavko, 2008, Seismic inversion combining rock physics and multiple-point geostaticstics: Geophysics, **73**, no. 1, R11–R21, doi: 10.1190/1.2803748.
Hale, E. T., W. Yin, and Y. Zhang, 2008, Fixed-point continuation for l_1-minimization: Methodology and convergence: SIAM Journal on Optimization, **19**, 1107–1130.
Hamid, H., and A. Pidlisecky, 2015, Multitrace impedance inversion with lateral constraints: Geophysics, **80**, no. 6, M101–M111, doi: 10.1190/geo2014-0546.1.
Hamid, H., A. Pidlisecky, and L. Lines, 2018, Prestack structurally constrained impedance inversion: Geophysics, **83**, no. 2, R89–R103, doi: 10.1190/geo2016-0703.1.
Hansen, T., K. Cordua, and K. Mosegaard, 2012, Inverse problems with non-trivial priors: Efficient solution through sequential Gibbs sampling: Computational Geoscience, **16**, 593–611, doi: 10.1007/s10596-011-9271-1.
Huang, W., R. Wang, Y. Chen, H. Li, and S. Gan, 2016, Damped multichannel singular spectrum analysis for 3D random noise attenuation: Geophysics, **81**, no. 4, V261–V270, doi: 10.1190/geo2015-0264.1.
Huang, W., R. Wang, X. Gong, and Y. Chen, 2017a, Iterative deblending of simultaneous-source seismic data with structuring median constraint: IEEE Geoscience and Remote Sensing Letters, **15**, 58–62, doi: 10.1109/LGRS.2017.2772857.
Huang, W., R. Wang, H. Li, and Y. Chen, 2017b, Unveiling the signals from extremely noisy microseismic data for high-resolution hydraulic fracturing monitoring: Scientific Reports, **7**, 1–16, doi: 10.1038/s41598-017-09711-2.
Huo, G., Q. Du, and X. Wang, 2017, AVO inversion constrained simultaneously in vertical and lateral directions: Chinese Journal of Geophysics, **60**, 271–282, doi: 10.6038/cjg20170122.
Jafarpour, B., V. Goyal, D. B. McLaughlin, and W. Freeman, 2009, Transform-domain sparsity regularization for inverse problems in geosciences: Geophysics, **74**, no. 5, R69–R83, doi: 10.1190/1.3157250.
Karimi, O., H. Omre, and M. Mohammadzadeh, 2010, Bayesian closed-skew Gaussian inversion of seismic AVO data for elastic material properties: Geophysics, **75**, no. 1, R1–R11, doi: 10.1190/1.3299291.
Karimi, P., 2015, Structure-constrained relative acoustic impedance using stratigraphic coordinates: Geophysics, **80**, no. 3, A63–A67, doi: 10.1190/geo2014-0439.1.
Liu, T., and T. K. Pong, 2017, Further properties of the forward-backward envelope with applications to difference-of-convex programming: Computational Optimization and Applications, **67**, 489–520, doi: 10.1007/s10589-017-9900-2.
Lou, Y., S. Osher, and J. Xin, 2015, Computational aspects of constrained L1-L2 minimization for compressive sensing: Journal of Infectious Diseases, **198**, 1327–1333, doi: 10.1007/978-3-319-18161-5_15.
Lou, Y., and M. Yan, 2016, Fast l1-l2 minimization via a proximal operator: Journal of Scientific Computing, **74**, 767–785, doi: 10.1007/s10915-017-0463-2.
Ma, M., S. Wang, and S. Yuan, 2017b, Multichannel spatially correlated reflectivity inversion using block sparse Bayesian learning: Geophysics, **82**, no. 4, V191–V199, doi: 10.1190/GEO2016-0366.1.
Ma, T.-H., Y. Lou, and T.-Z. Huang, 2017a, Truncated l_{1-2} models for sparse recovery and rank minimization: SIAM Journal on Imaging Sciences, **10**, 1346–1380, doi: 10.1137/16M1098929.
Mallick, S., 2001, AVO and elastic impedance: The Leading Edge, **20**, 1094–1104, doi: 10.1190/1.1487239.
Naghizadeh, M., and M. Sacchi, 2012, Multicomponent f-x seismic random noise attenuation via vector autoregressive operators: Geophysics, **77**, no. 2, V91–V99, doi: 10.1190/geo2011-0198.1.
Pérez, D. O., D. R. Velis, and M. D. Sacchi, 2013, High-resolution prestack seismic inversion using a hybrid FISTA least-squares strategy: Geophysics, **78**, no. 5, R185–195.
Porsani, M. J., 1999, Seismic trace interpolation using half-step prediction filters: Geophysics, **64**, 1461–1467.
Sacchi, M. D., and T. J. Ulrych, 1995, High-resolution velocity gathers and offset space reconstruction: Geophysics, **60**, 1169–1177.
She, B., Y. Wang, J. Liang, Z. Liu, C. Song, and G. Hu, 2018, A data-driven amplitude variation with offset inversion method via learned dictionaries and sparse representation: Geophysics, **83**, no. 6, R725–R748.
Siri, M. H., and C. V. Deutsch, 2018, Multivariate stochastic seismic inversion with adaptive sampling: Geophysics, **83**, no. 5, R429–R448.
Spitz, S., 1991, Seismic trace interpolation in the F-X domain: Geophysics, **56**, 785–794. doi: 10.1190/1.1443096.
Tao, P. D., and L. T. H. An, 1997, Convex analysis approach to D. C. programming: Theory, algorithms and applications: Acta Mathematica Vietnamica, **22**, 289–355.
Tao, P. D., and L. T. H. An, 1998, A DC optimization algorithm for solving the trust-region subproblem: SIAM Journal on Optimization, **8**, 476–505, doi: 10.1137/S1052623494274313.
Tikhonov, A. N., 1963, Solution of incorrectly formulated problems and the regularization method: Soviet Mathematical Doklady, **4**, 1035–1038.
Tikhonov, A. N., and V. Glasko, 1965, Use of the regularization method in nonlinear problems: USSR Computational Mathematics and Mathematical Physics, **5**, 93–107, doi: 10.1016/0041-5553(65)90150-3.
Varela, O. J., C. Torres-Verdín, and M. K. Sen, 2006, Enforcing smoothness and assessing uncertainty in non-linear one-dimensional prestack seismic inversion: Geophysical Prospecting, **54**, 239–259, doi: 10.1111/j.1365-2478.2006.00531.x.
Wang, J., and M. D. Sacchi, 2007, High-resolution wave-equation amplitude-variation-with-ray-parameter (AVP) imaging with sparseness constraints: Geophysics, **72**, no. 1, S11–S18, doi: 10.1190/1.2387139.
Wang, Y., 2002, Seismic trace interpolation in the f-x-y domain: Geophysics, **67**, 1232–1239.
Wang, Y., H. Zhou, X. Ma, and Y. Chen, 2018, L1-2 minimization for exact and stable seismic attenuation compensation: Geophysical Journal International, **213**, 1629–1646.
Yilmaz, O., 2001, Seismic data analysis: Processing, inversion, and interpretation of seismic data: SEG.
Yin, P., Y. Lou, Q. He, and J. Xin, 2015, Minimization of l_{1-2} for compressed sensing: SIAM Journal on Scientific Computing, **37**, A536–A563, doi: 10.1137/140952363.
Yuan, S., S. Wang, C. Luo, and Y. He, 2015, Simultaneous multitrace inversion with transform-domain sparsity promotion: Geophysics, **80**, no. 2, R71–R80.
Zhang, R., and J. Castagna, 2011, Seismic sparse-layer reflectivity inversion using basis pursuit decomposition: Geophysics, **76**, no. 6, R147–R158, doi: 10.1190/geo2011-0103.1.
Zhang, R., M. K. Sen, and S. Srinivasan, 2013, A prestack basis pursuit seismic inversion: Geophysics, **78**, no. 1, R1–R11, doi: 10.1190/geo2011-0502.1.
Zhang, T., 2010, Analysis of multi-stage convex relaxation for sparse regularization: Journal of Machine Learning Research, **11**, 1081–1107, doi: 10.1145/1756006.1756041.